MOROSIN, B. (1970). *Acta Cryst.* B**26**, 1635–1637.
MOROSIN, B. & SCHIRBER, J. E. (1965). *J. Chem. Phys.* **42**, 1389–1390.
NABOR, M. A., CALVERT, L. D. & WHALLEY, E. (1969). *J. Chem. Phys.* **51**, 1353–1356.
PAULING, L. (1960). *The Nature of the Chemical Bond,* 3rd ed., p. 464. Ithaca: Cornell Univ. Press.
SMITH, J. L., SCHIRBER, J. E. & MOROSIN, B. (1982). Private communication.
STEVENSON, R. (1961). *J. Chem. Phys.* **34**, 346–347.
SWENSON, C. A. & TEDESCHI, J. R. (1964). *J. Chem. Phys.* **40**, 1141–1143.
WORLTON, T. G., DECKER, D. L., JORGENSEN, J. D. & KLEB, R. (1986). *Physica,* **136B**, 503–506. Also *Neutron Scattering,* edited by G. H. LANDER & R. A. ROBINSON, pp. 503–506. Amsterdam: North-Holland.
ZACHARIASEN, W. H. (1927). *Z. Phys. Chem. (Leipzig),* **127**, 218–224.

Acta Cryst. (1989). B**45**, 218–227

Crystal Symmetry and Coherent Twin Structure of Calcium Zirconate

BY VINAYAK P. DRAVID, C. M. SUNG, M. R. NOTIS AND C. E. LYMAN

Department of Materials Science and Engineering, Lehigh University, Bethlehem, Pennsylvania 18015, *USA*

(*Received* 5 *July* 1988; *accepted* 11 *January* 1989)

Abstract

$CaZrO_3$ has been investigated at room temperature using a variety of electron microscopy techniques. Conventional transmission electron microscopy and high-resolution transmission electron miscroscopy revealed a characteristic coherent twin structure in $CaZrO_3$. In order to interpret the occurrence of the twin structure and the associated crystallography, the cell parameters and space-group symmetry of $CaZrO_3$ have been determined independently using convergent-beam electron diffraction. The results are consistent with those previously obtained by neutron diffraction. Both the crystal symmetry and lattice-parameter data have been used to explain the details of the twin structure in $CaZrO_3$.

Introduction

$CaZrO_3$ is a member of the large family of ABO_3 perovskite compounds. An ideal perovskite structure contains one formula unit and has a primitive cubic unit cell as shown in Fig. 1. Considerable attention has been given to the symmetry aspects of ABO_3 compounds and their close relationship with many engineering properties of these materials.

Structural studies of ABO_3 compounds are usually hampered by the difficulty of growing defect-free large single crystals. Furthermore, several ABO_3 compounds go through displacive and/or disorder–order phase transitions during cooling giving rise to domain structures. Therefore, there have been continual refinements of the crystal structure data of several ABO_3 compounds. (Tanaka, Saito & Tsuzuki, 1982; Vegas, Vallet-Regi, Gonzalez-Calbet & Alario-Franco, 1986).

$CaZrO_3$, in particular, has been the focus of only a small number of investigations (see Table 1). The first major study of ABO_3 compounds was conducted by Megaw (1946). She deduced from her powder X-ray diffraction (XRD) results that $CaZrO_3$ possessed orthorhombic symmetry at room temperature with cell parameters $a = 1{\cdot}1152$, $b = 0{\cdot}7994$ and $c = 1{\cdot}1492$ nm. The second major study was carried out by Coughanour, Roth, Marzullo & Sennett (1955) using powder XRD. They determined the room-temperature form of $CaZrO_3$ to be orthorhombic with lattice parameters $a = 0{\cdot}5587$, $b = 0{\cdot}8008$ and $c = 0{\cdot}5758$ nm. In addition, they mentioned that the $CaTiO_3$(and $CaZrO_3$)-type orthorhombic modification of ABO_3 compounds may not possess space group *Pcmn*, based upon their XRD intensity measurements. The most recent study is attributed to Koopmans, Van de Velde & Gellings (1983). They resorted to powder neutron diffraction for crystal structure and lattice-parameter determination of $CaZrO_3$ and $CaTiO_3$. They preferred the orthorhombic space group *Pcmn* over $Pc2_1a$ and *Amm*2, for both $CaZrO_3$ and $CaTiO_3$. The unit-cell parameters for $CaZrO_3$ were determined as:

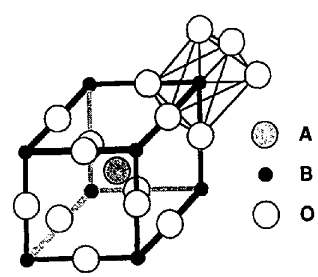

Fig. 1. Ideal perovskite structure of ABO_3-type compounds. Only one oxygen octahedron is emphasized.

0108-7681/89/030218-10$03.00

Table 1. *Structural studies of* $CaZrO_3$

Reference	Technique	Results and comments
Megaw (1946)	Powder XRD	Orthorhombic symmetry was deduced with cell parameters $a = 1{\cdot}1152$, $b = 0{\cdot}7994$ and $c = 1{\cdot}1492$ nm; a and c axial lengths are double the accepted ones.
Coughanour *et al.* (1955)	Powder XRD	Orthorhombic symmetry was confirmed. Cell parameters $a = 0{\cdot}5587$, $b = 0{\cdot}8008$ and $c = 0{\cdot}5758$ nm. The accepted space group *Pcmn* was questioned.
Koopmans *et al.* (1983)	Powder neutron diffraction	Cell parameters in agreement with Coughanour *et al.* *Pcmn* space group of $CaTiO_3$ and $CaZrO_3$ was confirmed and atomic coordinates established.
Foex *et al.* (1967)	High-temperature XRD	Phase transition from cubic to orthorhombic symmetry at about 2023 K was noted.
Stubican (1986)	High-temperature XRD	Primitive cubic form at high temperature was confirmed. Phase transition at about 2023 K was confirmed.
This study	CBED on twinned single crystals	Cell parameters in agreement with Coughanour *et al.* and Koopmans *et al.* Direct confirmation of the assigned space group *Pcmn*. Twin-boundary crystallography discussed.

$a = 0{\cdot}55912\ (1)$, $b = 0{\cdot}80171\ (2)$ and $c = 0{\cdot}57616\ (1)$ nm. They also attributed the differences in their structural data and the previous data of Kay & Bailey (1957) to large-scale twinning in $CaTiO_3$. Since twinning is also ubiquitous in room-temperature $CaZrO_3$, similar differences may occur in $CaZrO_3$. In addition, the JCPDS card No. 20-254 defines $CaZrO_3$ as cubic at $\sim$2223 K which is quite consistent with Stubican's (1986) recent high-temperature XRD results; however, card No. 9-364 considers $CaZrO_3$ as calcium *meta*-zirconate with no mention of space group. This card defines calcium *meta*-zirconate as orthorhombic with a monoclinic pseudocell and the large unit-cell orthorhombic parameters have been adapted from Megaw (1946). This particular card also has a confusing comment 'perovskite-type lattice, pseudocubic at room temperature'. However, the recent version of this card incorporates the data of Koopmans *et al.* (1983).

Therefore in order to resolve these ambiguities, we have performed a complete characterization of single-crystal $CaZrO_3$ in the form of a eutectic phase in the directionally solidified eutectic (DSE), ZrO_2(ss)–$CaZrO_3$. Emphasis in this paper has been placed on the cell parameters and symmetry of $CaZrO_3$, and the use of these in interpreting the domain structures observed in this study.

Experimental

The DSE sample in the system CaO–ZrO_2 consists of regular alternate lamellae of the stoichiometric line compound $CaZrO_3$ and CaO-stablized cubic ZrO_2(ss). Thin slices were cut from the bulk sample and conventional mechanical polishing, dimpling and ion-beam thinning techniques were used to obtain electron-transparent foils. A thin layer of amorphous carbon was then deposited on the thin foils to avoid charging effects. Stoichiometric $CaZrO_3$ powder was also used to confirm convergent-beam electron diffraction (CBED) results from the DSE sample. The $CaZrO_3$ powder was annealed several times at 1773 K for 8 h. The powder was then crushed using a mortar and pestle. Thin fragments of $CaZrO_3$ were floated on a holey carbon film supported by a copper grid for subsequent CBED studies. The CBED results obtained from both types of samples were identical; therefore only the results from the bulk samples are described in this paper.

The CBED study was conducted at 120 kV using a Philips EM 400T microscope. Conventional transmission electron microscopy (CTEM) and high-resolution transmission electron microscopy (HRTEM) experiments were performed using a Philips EM 430T operated at 250 kV. For CBED, a probe size of about 10 nm was used and all the HRTEM images in this paper were obtained near the Scherzer defocus (−80 nm) as determined from optical diffraction. One of the first approaches described by Ecob, Shaw, Porter & Ralph (1981) for indexing the higher-order Laue zone (HOLZ) reflections did not simulate all the observed HOLZ lines. Therefore a more complete program for indexing all the observed HOLZ reflections based on kinematical conditions has been developed using the visibility criterion originally developed for Kossel lines (Biggin & Dingley, 1977). This approach is easy and more accurate. With this technique we have been able to use HOLZ lines from low-symmetry zone axes and simulate these patterns in order to measure lattice-parameter changes through HOLZ-line shifts (Sung & Williams, 1987).

Results

Fig. 2 shows a transmission optical image of the DSE depicting the typical lamellar morphology; the lighter phase is $CaZrO_3$ and the darker phase is ZrO_2(ss). A

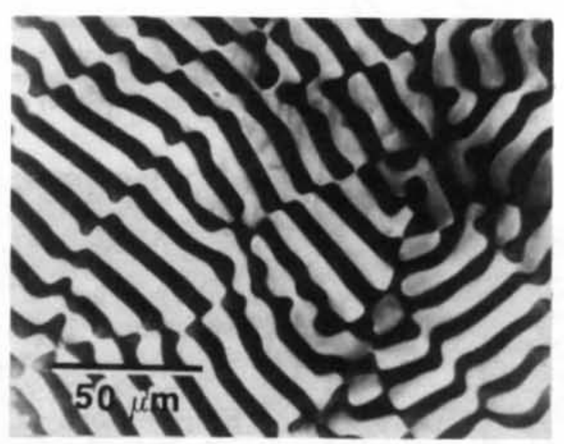

Fig. 2. Transmission optical micrograph of $CaZrO_3$(lighter phase)–ZrO_2(darker phase) DSE, depicting the typical lamellar morphology.

characteristic domain structure was observed in the $CaZrO_3$ phase when imaged in strong diffraction conditions as shown in Fig. 3. Twin-like boundaries seen edge-on are denoted by 'TBs', while inclined boundaries exhibiting fringe contrast are denoted by δ. The asymmetric fringe contrast in this image is a characteristic of δ-boundary fringe contrast, often associated with coherent twins under certain diffraction conditions (Amelinckx & Van Landuyt, 1978).

The presence of the twin structure suggests that $CaZrO_3$ has gone through a phase transition. In order to understand the nature and crystallography of these domains, it was necessary to first determine the space-group symmetry of $CaZrO_3$ as it appeared in the domain structure. Therefore, CBED was performed on single domains in several orientations.

Point-group determination

Fig. 4 shows three different portions of the CBED pattern: the whole pattern (WP), its corresponding zero-order Laue zone (ZOLZ) pattern and the bright-

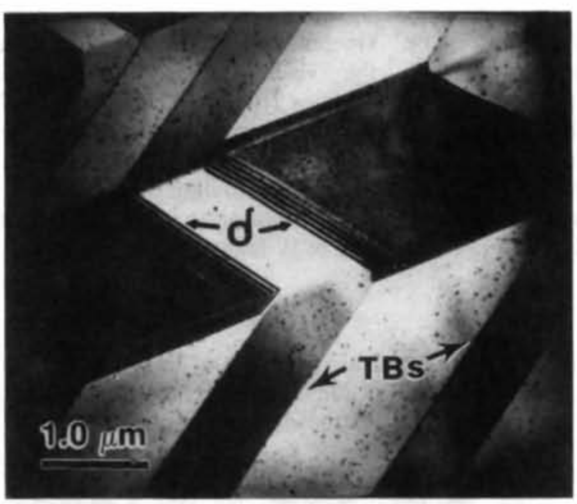

Fig. 3. Bright-field image of $CaZrO_3$ domain structure in a strong diffraction condition. Edge-on twin boundaries are indicated by 'TBs' and typical δ boundary fringe contrast is denoted by δ.

Table 2. *Pattern symmetries in* $CaZrO_3$

Zone axis	Projection diffraction symmetry	Bright field	Whole pattern	Deduced diffraction groups
[100]	$2mm$	$2mm$	$2mm$	$2mm1_R/2mm$
[010]	$2mm$	$2mm$	$2mm$	$2mm1_R/2mm$
[001]	$2mm$	$2mm$	$2mm$	$2mm1_R/2mm$
[101]	$2mm$	m	m	$2_Rmm_R/m$
[011]	$2mm$	m	m	$2_Rmm_R/m$
[110]	$2mm$	m	m	$2_Rmm_R/m$

Point group '*mmm*'.

field (BF) pattern from the (000) spot of $CaZrO_3$. This orientation was later recognized as [010]. The WP, BF and projection diffraction symmetries (PDS) are all $2mm$. Thus, with reference to the tables of Buxton, Eades, Steeds & Rackham (1976), the crystal possesses either diffraction group $2mm1_R$ or $2mm$. Two other high-symmetry CBED patterns, similar to above (later recognized as [100] and [001]), also exhibited the same diffraction groups. Furthermore, no other zone axis with symmetries higher than $2mm$ could be found and the above three zone axes were mutually perpendicular, within the accuracy of the goniometer tilts ($\pm\frac{1}{2}°$) of the microscope. Defining the unit-cell axes along the three orthogonal directions, the above observations confirm the Bravais lattice of $CaZrO_3$ to be orthorhombic since only orthorhombic crystals can have $2mm$ symmetry in three mutually orthogonal directions. In orthorhombic crystals, only crystals of the *mmm* point group show $2mm1_R/2mm$ diffraction groups in three different zone axes (Buxton *et al.*, 1976). Further, other zone axes also showed symmetries expected from the *mmm* point group as summarized in Table 2. Thus with reference to Table 2, the point group of $CaZrO_3$ is established as *mmm*.

The unit-cell type of orthorhombic $CaZrO_3$ was readily determined by overlaying the first-order Laue zone (FOLZ) reflections onto the ZOLZ reflections for all of the above three $\langle 010 \rangle$-type zone axes. When this was done, the FOLZ reflections superimposed (within the measuring accuracy: $\geq$90%) onto the ZOLZ, indicating that the unit cell in reciprocal space is primitive. Thus,

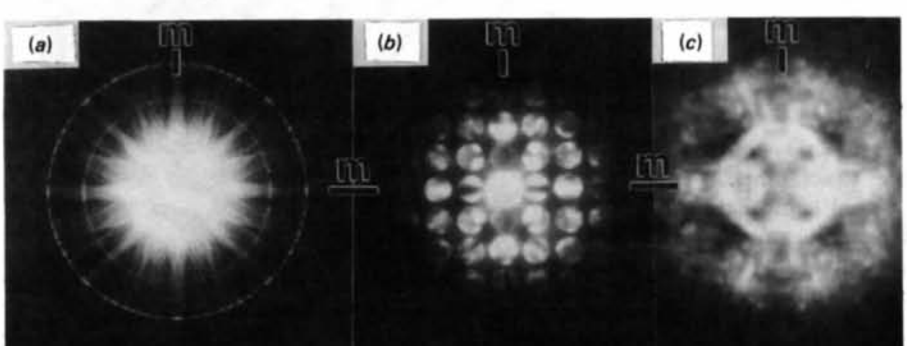

Fig. 4. [010] Zone-axis pattern from $CaZrO_3$. (*a*) WP, (*b*) ZOLZ and (*c*) BF disc. All the patterns possess '$2mm$' symmetry. Note the orthogonal G–M lines along $00l$ and $h00$.

the real-space unit cell will also be primitive. The above discussion alone rules out two space groups considered by Koopmans *et al.* (1983): $Pna2_1$, which has $mm2$ point group and $Amm2$, which in addition is not primitive.

Space-group determination

The additional translation symmetry elements such as screw axes/glide planes necessary to determine the space group were then deduced by observing the dynamical absences in the kinematically forbidden reflections in CBED patterns. The dynamical absences or G–M lines appear as dark bands in some kinematically forbidden reflections (Gjonnes & Moodie, 1965), which indicates that the electron beam is either parallel to a glide plane or perpendicular to a screw axis. Steeds & Vincent (1983) have noted some specific characteristics of G–M lines, which were used as guidelines in the present study to confirm their presence. Briefly, these are as follows:

(1) Alternate (forbidden) reflections along a systematic row must show the G–M lines.

(2) The G–M lines persist at all voltages and thicknesses though their width decreases with increasing thickness (provided that the double diffraction route is still available).

(3) A 'black cross' of G–M lines should be seen at the exact Bragg condition of the forbidden reflections (within ZOLZ, from ZOLZ).

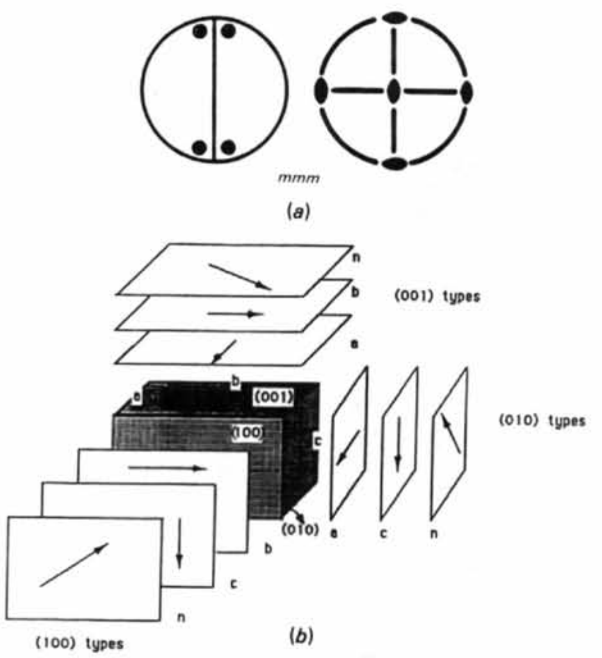

Fig. 5. (*a*) Stereographic projection of *mmm* point group, depicting the orientation of twofold rotation/screw axes and (*b*) location of possible glide planes in *mmm* point group.

The three-dimensional effects in the BF disc (HOLZ line symmetry) were used in deducing the presence of symmetry elements responsible for the G–M lines. For the *mmm* point group, only twofold screw/rotation axes and (100)-, (010)- and (001)-type glide/mirror planes are possible as seen from Fig. 5. Fig. 4 has $2mm$ BF symmetry (HOLZ line symmetry) and also possesses the G–M lines in alternate reflections in two orthogonal rows ($00l$, $h00$; $h,l \neq 2n$). Thus, according to Steeds & Vincent (1983), the minimum number of symmetry elements responsible for the G–M lines are two mutually perpendicular glide planes, but it is not possible to identify the symmetry element responsible for each set of dynamic absences. Therefore, we have employed particular zone-axis CBED patterns to single out, unambiguously, the symmetry elements responsible for the specific dynamic absences; rather low-symmetry zone axes with three-dimensional effects in the BF discs were used. The determination of the presence of screw axes and/or glide planes can then be carried out by locating the position of G–M lines with respect to the BF mirror.

Since the *mmm* point group may consist of only twofold screw/rotation axes and (100), (010) and (001) glide planes, $\langle uv0\rangle$-, $\langle u0w\rangle$- and $\langle 0vw\rangle$-type zone axes are most appropriate for investigation as the BF symmetry of these axes for the *mmm* point group corresponds to a single mirror 'm', and HOLZ lines are visible and sharp along such zone axes. Therefore

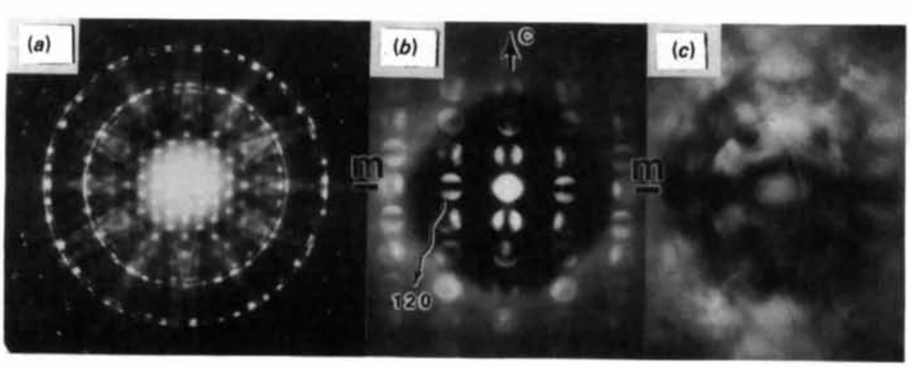

Fig. 6. [$\bar{2}$10] Zone-axis pattern. (*a*) WP, (*b*) ZOLZ and (*c*) BF disc. G–M lines are present along ($00l$), $l \neq 2n$ systematic row and along ($hk0$), $h + k \neq 2n$ reflections.

unambiguous determination of the presence of screw axes/glide planes is possible as will be discussed below.

Fig. 6 shows the $[\bar{2}10]$ zone-axis CBED patterns from $CaZrO_3$. The BF and the WP symmetry is only 'm'. There are G–M lines in alternate reflections along the systematic $00l$ ($l \neq 2n$) row, *e.g.* (001) and in $\{hk0\}$, $h+k \neq 2n$, *e.g.* $\pm$ (120) discs. Because the $(00l)$, $l \neq 2n$ G–M lines are orthogonal to the BF mirror plane 'm', they are attributed clearly to a [001] screw axis, and the G–M lines in $\pm(hk0)$ reflections, *e.g.* $\pm(120)$, being parallel to the BF mirror, occur as a result of a (001) n-glide plane which is perpendicular to the [001] screw axis (Gjonnes & Moodie, 1965). Fig. 7 is the [011] zone-axis pattern (ZAP) where the BF disc again has only 'm' symmetry. Thus $(h00)$, $h \neq 2n$ G–M lines occur clearly due to a [100] screw axis and $(0kl)$, $l \neq 2n$ G–M lines are a consequence of a (100) c-glide plane. Finally, the [101] ZAP is presented in Fig. 8. In this ZAP there are G–M lines only along $(0k0)$, $k \neq 2n$ systematic row, but they are difficult to see owing to the short reciprocal vector of $(0k0)$ reflections. However, the presence of G–M lines could easily be confirmed by satisfying Bragg's law for $(0k0)$, $k \neq 2n$ reflections such as $(0\bar{7}0)$ where a black cross is clearly seen in Fig. 8(*c*). Thus these G–M lines, following the previous arguments, could only result from a [010] screw axis and a mirror plane perpendicular to it could be inferred. No evidence for a (010) glide plane was obtained.

So far we have analyzed three $\langle uv0 \rangle$-type patterns with two symmetry elements associated with three orthogonal axes, *viz.* $2_1/c$, $2_1/m$ and $2_1/n$ (c, n being glide planes) and we have also determined the unit-cell type as primitive. Further, the rule of forbidden reflections observed in this study may be summarized as:

$$hkl\text{: no condition} \qquad h0l\text{: no condition}$$
$$hk0\text{: } h+k=2n \qquad 0kl\text{: } l=2n$$

and

$$\left.\begin{array}{r} h00 \\ 0k0 \\ 00l \end{array}\right\} \quad h,k,l=2n$$

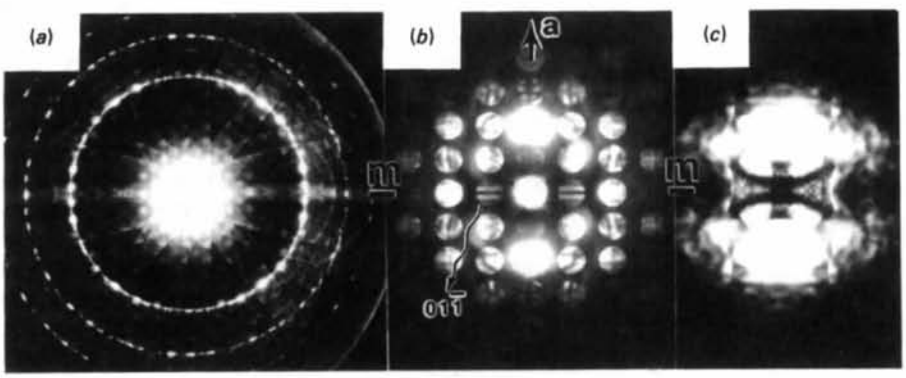

Fig. 7. [011] Zone-axis pattern. (*a*) WP, (*b*) ZOLZ and (*c*) BF disc. Orthogonal G–M lines can be seen within $(h00)$, $h \neq 2n$ and $(0kl)$, $l \neq 2n$ discs.

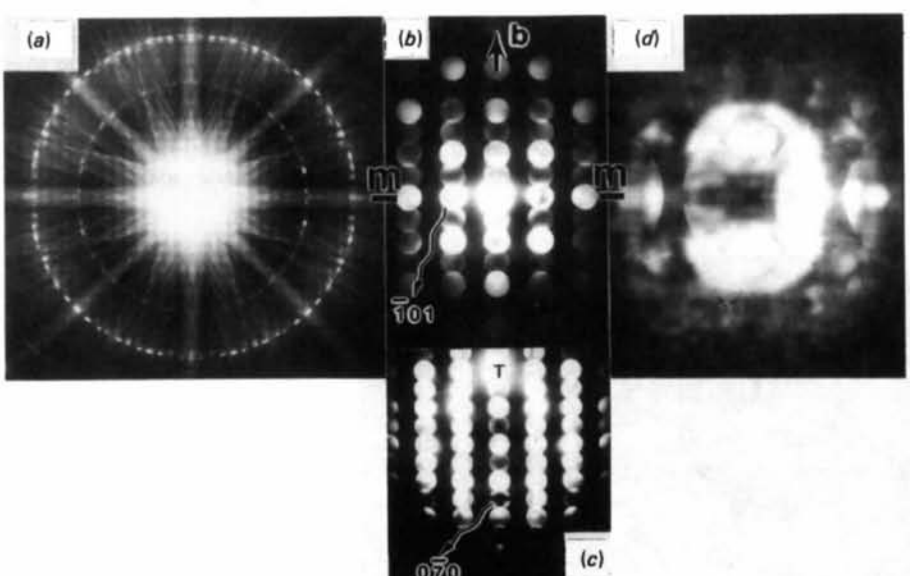

Fig. 8. [101] Zone-axis pattern. (*a*) WP, (*b*) ZOLZ, (*c*) Bragg law has been satisfied for $(0\bar{7}0)$, where a black cross is clearly seen (see text) which indicates $(0k0)$, $k \neq 2n$ G–M lines, and (*d*) BF disc.

The above analysis conforms to the space group *Pcmn*, No. 62, of *International Tables for Crystallography* (1983), which is in agreement with Koopmans *et al.* (1983).

Lattice-parameter determination

When a convergent electron beam illuminates the specimen the diffraction pattern consists of discs, the diameter of which depends upon the convergence angle. The detailed contrast effects seen in CBED patterns consist of diffuse scattering within the discs and sharp lines which are visible both within the discs and outside them. The lines within the HOLZ and BF discs arise from three-dimensional diffraction and are the result of elastic scattering by the planes in the HOLZ. HOLZ lines were first reported and discussed by Jones, Rackham & Steeds (1975). The basic idea of the origin of HOLZ lines may be explained by purely kinematical arguments, although the dynamical theory of electron diffraction is required to describe accurately their position, intensity and fine structure.

In principle, at orientations where only weak interactions between zero and higher-layer Bloch waves take place, the branches of the dispersion surface corresponding to the HOLZ Bloch wave lie very close to a dispersion sphere, of radius corrected for the mean potential, and centered on the HOLZ reciprocal lattice point. Hence, approximate positions for the HOLZ lines can be found by calculating orientations at which dispersion spheres intersect the zero-layer dispersion surface. These intersections give a geometrical position for the HOLZ lines. The large radius of the Ewald sphere [due to high accelerating voltage (120 kV)], in comparison with the spacing of reciprocal lattice points, implies that the range of incident-beam directions over which excitation of the higher-order beam can take place must be very small. Small changes in the radius of the Ewald sphere or in the spacing of reciprocal lattice points cause large changes in the position of the HOLZ lines. Thus the effect of changes in the accelerating voltage or specimen lattice parameter can result in the HOLZ line shifts.

Having established the space group of $CaZrO_3$ as *Pcmn*, lattice parameters were obtained by comparing HOLZ lines on the [140] and [043] zone axes with computer-simulated HOLZ lines as seen in Figs. 9 and 10. Until recently, the study of lattice parameter determination by HOLZ line simulation has been focused on high-symmetry zone axes in cubic or

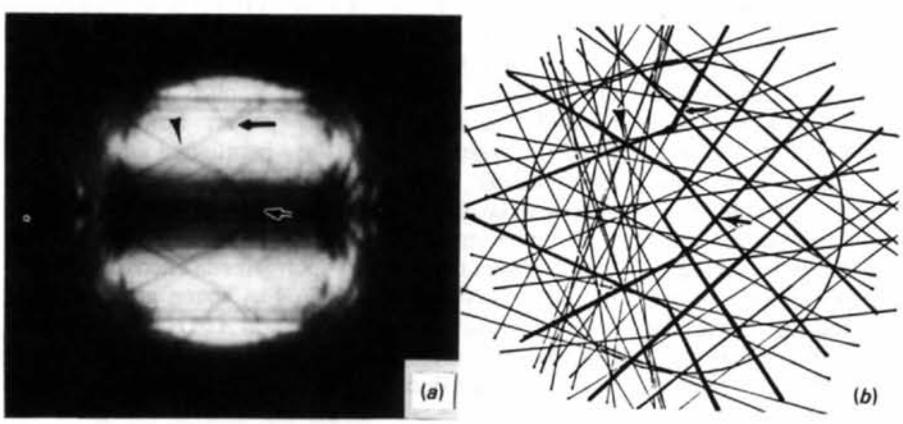

Fig. 9. (*a*) BF disc in [140] orientation showing a network of HOLZ defect lines and (*b*) computer-simulated HOLZ line match for (*a*). Note that '*m*' symmetry is well preserved in both the patterns. $a = 0{\cdot}559$, $b = 0{\cdot}802$ and $c = 0{\cdot}576$ nm. Arrows indicate main features corresponding to (*a*) and (*b*).

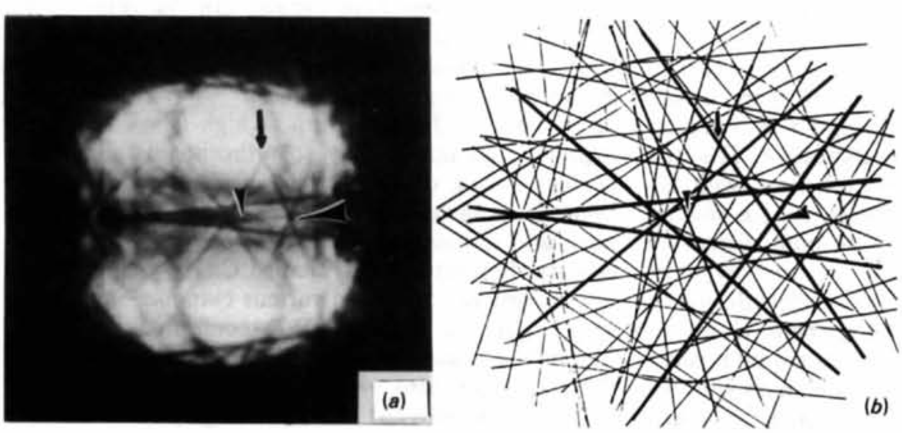

Fig. 10. Similar to Fig. 9, except in [043] orientation.

close-packed hexagonal systems (Ecob *et al.*, 1981; Shelton, Porter & Ralph, 1983). It is difficult to obtain sharp and clear HOLZ lines from high-symmetry zone axes in orthorhombic $CaZrO_3$ at room temperature owing to strong dynamical interactions within the ZOLZ. Nevertheless, we have observed HOLZ lines of high-index low-symmetry zones in addition to high-symmetry zones. It was then possible to simulate HOLZ lines using a computer program assuming kinematical conditions (Sung & Williams, 1987). Figs. 9 and 10 show the experimental BF discs along the [140] and [043] zone-axis patterns depicting the HOLZ defect line positions and their corresponding computer-simulated patterns. An excellent match was obtained for $a = 0{\cdot}559$, $b = 0{\cdot}802$ and $c = 0{\cdot}576$ nm within 0·1% error. These values are in good agreement with the recent X-ray diffraction data of Koopmans *et al.* (1983), *i.e.* $a = 0{\cdot}55912$, $b = 0{\cdot}80171$ and $c = 0{\cdot}57616$ nm. However, it should be noted that it is difficult to see the matched HOLZ patterns clearly between experimental and simulated ones owing to the significant contribution of dynamical scattering to HOLZ lines.

One of the main problems in investigating the use of HOLZ line analysis is that of deciding which zone axis is most sensitive to lattice-parameter changes. For instance, Ecob *et al.* (1981) chose the $\langle 111 \rangle$ zone axes in an f.c.c. system even though it is difficult to obtain HOLZ lines along high-symmetry low-index zone axes owing to their sensitivity to crystal symmetry and lattice parameters. It is necessary to find a zone-axis pattern which contains a small number of HOLZ lines which are easily visible, and especially which show notable changes at their cross point as a result of the lattice-parameter changes. Using the kinematical analysis, the lines in patterns from the high-symmetry zone axes were consistent (within 1%) with an assumed value of the electron wavelength, and therefore, the accelerating voltage. Nevertheless, it should be noted that different materials require different assumed accelerating voltages in order to obtain best matching. However, the voltage required to match the simulation of the experimental patterns for certain high-index low-symmetry zone axes was about 5–6% higher or lower than the voltage for low-index high-symmetry zone axes obtained under the same microscope conditions. It should be noted that this program is based on the kinematic approach to electron diffraction. Thus the Ewald sphere is assumed to be spherical with no perturbations due to dispersion effects. As the simulation technique does not take into account dispersion effects, it is necessary to perform some type of calibration of the effective electron wavelength, which may be different from the actual wavelength. However, for $CaZrO_3$ we did not find any significant differences in HOLZ line simulation at various zone axes with the same voltage. For example, the low-symmetry zone axis of [214] was observed and the simulation of these HOLZ lines resulted in the same values of lattice parameters as obtained from the higher-symmetry zone axis of [140].

Discussion

It is well known that many ABO_3 compounds possess the ideal perovskite structure (space group $Pm\bar{3}m$) at high temperatures due to the dominating effect of the entropy term which dictates the high-temperature lattice form. The ideal perovskite unit cell consists of corner-shared oxygen octahedra with B cations at their centers and A cations residing in the cubooctahedral interstices. However, as the temperature is lowered, the lattice instability results in lowering of the space-group symmetry of many of these compounds. The reasons for this instability are many but it is usually attributed to either a small displacement of cations or tilting of the oxygen octahedra or a combination of both. An elegant scheme for classifying octahedral tilting in perovskites has been proposed by Glazer (1972), which is based on a description of the distortion of the perovskite structure by a combination of rotations about $\langle 010 \rangle_p$ (hereafter subscript 'p' corresponds to the 'aristotype' perovskite structure). This description was further extended by O'Keeffe & Hyde (1977) to some specific cases related to perovskites. The complete description of the methodology and analysis of Glazer (1972) and O'Keeffe & Hyde (1977) as applied to $CaZrO_3$, is beyond the scope of this paper; however, many important results of the above-mentioned analysis may be applicable, at least qualitatively, to $CaZrO_3$ and are described later in this section.

Detailed structural investigation of $CaZrO_3$ at high temperatures has not been performed. There is evidence that at $\geq\sim$2023 K, $CaZrO_3$ has space group $Pm\bar{3}m$, which is isostructural with several ABO_3 compounds at high temperatures. However, except at ~2023 K where a phase transition has been noted (Stubican, 1986; Foex, Traverse & Coutures, 1967), no other investigations have been performed below ~2023 K and below room-temperature ranges. On the other hand, $CaTiO_3$ and $SrZrO_3$, which are isostructural with $CaZrO_3$ at room temperature, have been investigated in several temperature ranges. $CaTiO_3$ has ideal perovskite ($Pm\bar{3}m$) structure at high temperature and departs from this slightly to orthorhombic symmetry ($Pcmn$) during cooling. Unlike $CaZrO_3$, $CaTiO_3$ has been investigated extensively using a variety of analytical techniques. As early as the beginning of this century, Bowman (1908) studied $CaTiO_3$ using optical microscopy and observed various twin-like boundaries. Later, Kay & Bailey (1957) confirmed the orthorhombic symmetry of synthetic as well as natural $CaTiO_3$. They also proposed space group $Pcmn$ for $CaTiO_3$ and analyzed the crystallography of the twin boundaries. Their twin-boundary results have been recently confirmed by White, Segall, Barry & Hutchison (1985). $SrZrO_3$ has been investigated in detail by Ahtee, Glazer & Hewat (1978). They proposed that it goes through several phase transitions during cooling from temperatures > 1443 K. However, at room temperature, it possesses *Pbnm* symmetry [$a = 0{\cdot}57862\,(5)$, $b = 0{\cdot}58151\,(6)$ and $c = 0{\cdot}81960\,(8)$ nm]. We have confirmed that the room-temperature space group of $SrZrO_3$ is *Pbnm* using CBED and have observed the characteristic twin-boundary structure. Thus, many ABO_3 compounds are observed to possess characteristic domain boundaries at room temperature.

The observation of domain boundaries is not surprising since it is well documented that during many phase transitions, especially second-order phase transitions, such as disorder–order and displacive, the high-temperature (usually) higher-symmetry form of the crystal transforms to a low-temperature lower-symmetry form (Amelinckx & Van Landuyt, 1978). The lowering of symmetry results in some lost symmetry elements of the higher-symmetry form, which manifest themselves as domain boundaries after the phase transition. Therefore, if the phase transition is such that the high-symmetry space group is a supergroup of the low-symmetry space group, then the domain structure crystallography can be readily predicted by the space-group theoretical approach (Van Tendeloo & Amelinckx, 1974; Guymont, Gratias, Portier & Fayard, 1976) under a few constraints. However, since $CaZrO_3$ has not been investigated in the high-temperature range where another phase transition is possible, the space-group theoretical approach may not be directly applicable. Nevertheless, for a phase transition from $m\bar{3}m$ to mmm point group, the theory of Van Tendeloo & Amelinckx (1974) predicts six orientational variants. The number of 'different' interfaces corresponds to the number of classes of a variant generating group (VGG) in G, the high-symmetry point group. The calculations, presently underway, indicate two different types of twin boundaries.

Glazer (1972) and O'Keeffe & Hyde (1977), on the other hand, have shown that many low-symmetry structures based on ABO_3 can be derived from the 'aristotype' (parent) ideal perovskite using systematic topological distortions. They investigated several possible low-symmetry structures based on ideal perovskite and deduced the possible octahedral distortions using Glazer (1972) notations. However, they did not specify in what manner the distortions would be accommodated in the derived structure. Nevertheless, what is implicit in their analysis is that some distortion must be accommodated by lattice defects such as twin boundaries. Further, their topological distortion scheme is also useful when describing the twin-boundary crystallography.

Having determined the room-temperature crystal form of $CaZrO_3$ to be orthorhombic and lattice parameters as $a = 0{\cdot}559$, $b = 0{\cdot}802$ and $c = 0{\cdot}576$ nm, the orthorhombic cell can be generated from the pseudocubic structure as shown in Fig. 11, which is the (010) projection of four pseudocubic cells. The orthorhombic cell parameters compare with those of parent cubic cell parameters as: $a_o \simeq \sqrt{2}a_c$, $b \simeq 2b_c$ and $c_o \simeq \sqrt{2}c_c$. One can envisage the creation of the orthorhombic cell from the pseudocubic cell by the matrix transformation:

$$\begin{pmatrix} a_o \\ b_o \\ c_o \end{pmatrix} = \begin{pmatrix} 1 & 0 & \bar{1} \\ 0 & 2 & 0 \\ 1 & 0 & 1 \end{pmatrix} \begin{pmatrix} a_c \\ b_c \\ c_c \end{pmatrix}$$

where a_o, b_o, c_o are the unit-cell vectors of the orthorhombic cell and a_c, b_c and c_c are unit-cell vectors of the parent unit cell.

Using the above information, one can easily deduce the interface planes associated with the domain boundaries such as in Fig. 3. Fig. 12 shows another set of domain structures in $CaZrO_3$ in almost 'edge-on' orientation. These boundaries can be identified as 90° and 180° rotation twin boundaries along $\langle 101 \rangle$, with twin planes being (101) and (10$\bar{1}$). (100) twin planes were occasionally observed. However, as noted by Dravid, Notis & Lyman (1987), the (100) twin-boundary plane was quite diffuse and thus may not be strictly (100). The details of the twin boundaries are reported elsewhere (Dravid *et al.*, 1987), but a typical selected-area electron-diffraction (SAED) pattern (zone axis [010]) taken on a (101) twin interface is shown in Fig. 12. It displays an unsplit row of ($h0h$) reflections which is normal to the twin plane (101), and spot splitting (arrows) is evident in the rows which are parallel to the unsplit row. This situation is clear evidence of a reflection twin on (101), or more precisely a 180°

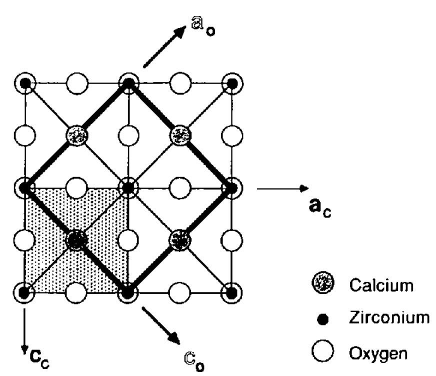

Fig. 11. (010)-Projection of four pseudocubic cells of $CaZrO_3$. Lattice correspondence between the pseudocubic cell (shaded square) and the orthorhombic cell (thick outline) is indicated. The $\bar{b}$ axis of the orthorhombic cell is double the $\bar{b}$ axis of the pseudocubic, which is normal to the plane of the paper.

rotation about (101), keeping the *b* axes of both the crystals antiparallel. The twin obliquity angle θ is quite large, about $3{\cdot}5 \pm 0{\cdot}5°$, based on SAED and CBED measurements.

The principal contrast associated with the twin boundaries is the δ-boundary fringe contrast, where the fringe profile is asymmetric in the bright-field images and is symmetric in the corresponding dark-field images. The δ fringe contrast has been observed in the case of $CaZrO_3$ twin boundaries (Fig. 3) and has been discussed in detail by Dravid *et al.* (1987). When the lattice parameters (*a*, *b* and *c*) of room-temperature $CaZrO_3$ are compared with that of high-temperature cubic phase, one can deduce that $a_o = \sqrt{2}a_c$, $b_o \simeq 2a_c$ and $c_o \simeq \sqrt{2}a_c$, which implies that a finite rotation of oxygen octahedra and (probably) a finite cationic displacement are necessary to conform to *Pcmn* symmetry. We suggest that the distortions are accommodated by introducing twinning mainly on (101) and $(10\bar{1})$ of the orthorhombic phase [that is, (001) and (100) of pseudocubic cell, see Fig. 11]. The occurrence of 90° and 180° rotation twins about $\{101\}$ of the orthorhombic phase is compatible with the Glazer derivation. For the $CaZrO_3$ *Pcmn* setting, the three-tilt system (assuming no cationic displacement) becomes $a^-b^+a^-$, where two octahedral tilts (a^-) are in antiphase but in the same sense, and one octahedral tilt (b^+) is in phase. This tilt system appears feasible since Koopmans *et al.* (1983) have noted substantial rotation of ZrO_6 octahedra. Further, as noted by O'Keeffe and Hyde (1977), the group of operations in the case of space group *Pcmn* involves $\langle 100 \rangle$-type rotation axes in the parent phase (within $\{011\}_p$ planes) which is again compatible with the twinning observations in this study. Twinning along (100) of orthorhombic phase has also been observed, but rather infrequently. This may be due to the fact that perfect regularity of the octahedra is incompatible with fixed rotation axes; a primary rotation implies the necessity of a secondary tilt (O'Keeffe & Hyde, 1977). Thus, predominant twin planes in $CaZrO_3$ are observed to be $\{101\}$ and occasionally (100). However, until now, no evidence has been obtained for $\{121\}$ twin planes, which were observed by White *et al.* (1985) in the case of $CaTiO_3$.

The twin interfaces were observed to be fully coherent which implies that the juxtaposition of opposite senses of octahedral tilts across the twin boundary is necessary to avoid any appreciable displacements of ions at the interfaces. Fig. 13 shows an HRTEM image, a (101) twin interface in $CaZrO_3$. The twin plane (101) is fully coherent with a finite bending of lattice planes across it, which accommodates the transformation strain. Unlike the observations of White *et al.* (1985) in the case of $CaTiO_3$, we did not observe any fine-scale intergrowth or defects at these interfaces. However, occasionally, excessive strain at the twin junctions appears to be accommodated by small-angle grain boundaries and asymmetric planar interfaces (Fig. 14).

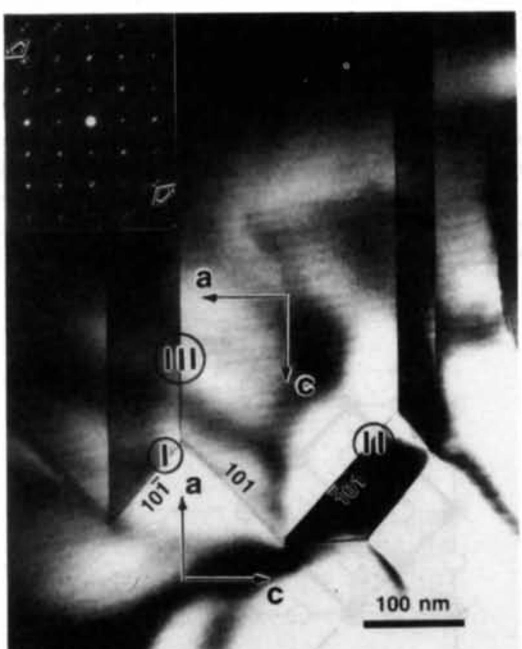

Fig. 12. Twin-boundary domain structure in $CaZrO_3$. Three types of twin boundaries are indicated by I, II and III. Inset is the selected-area diffraction pattern taken from a (101) twin segment along a [010] zone axis. Spot splitting is evident (arrows), parallel to the unsplit *h0h* systematic row. The unsplit row is perpendicular to the (101) twin plane.

Summary

In agreement with the results of Koopmans *et al.* (1983), the room-temperature crystal symmetry of

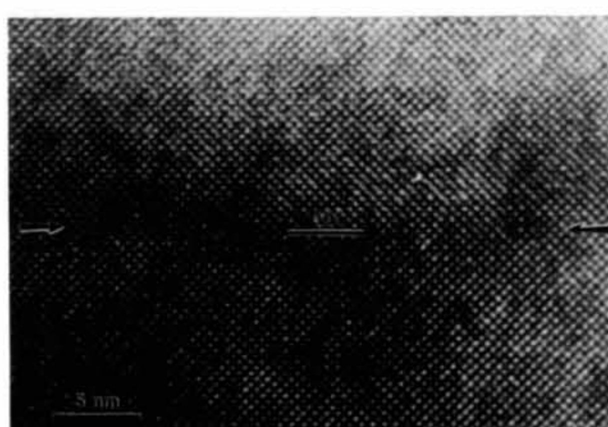

Fig. 13. An HRTEM image of a (101) twin boundary of Fig. 12. Note that the twin plane is exactly (101), with no evidence of defects or intergrowth at the interface. Slight bending of the lattice planes is apparent.

$CaZrO_3$ is determined using CBED to be *Pcmn*. The space-group determination by CBED is greatly facilitated by analyzing patterns which display three-dimensional symmetry (HOLZ line symmetry) within the BF discs. The three-dimensional diffraction effects can also be used to obtain lattice-parameter data from small volumes with acceptable accuracy even in complicated crystal structures such as the one presented in this paper. This can be achieved by comparing observed HOLZ defect lines in the BF disc with those of computer-simulated ones. Extensive twinning was observed in 'single-crystal' $CaZrO_3$. The occurrence of twin domains can be rationalized by taking into account the transformation strain and the lowering of symmetry during cooling from the high-temperature high-symmetry crystal form of $CaZrO_3$. One of the direct consequences of the topological distortion of BO_6 octahedra for deriving lower-symmetry structures, as proposed by Glazer (1972) and O'Keeffe & Hyde (1977), appears to be twinning in the present case. Preliminary analysis shows that twinning on {101} effectively accounts for the topological distortion in the room-temperature crystal form of $CaZrO_3$, analogous to that in $CaTiO_3$. However, a cogent interpretation awaits detailed investigations in the high-temperature range, which may involve another phase transition.

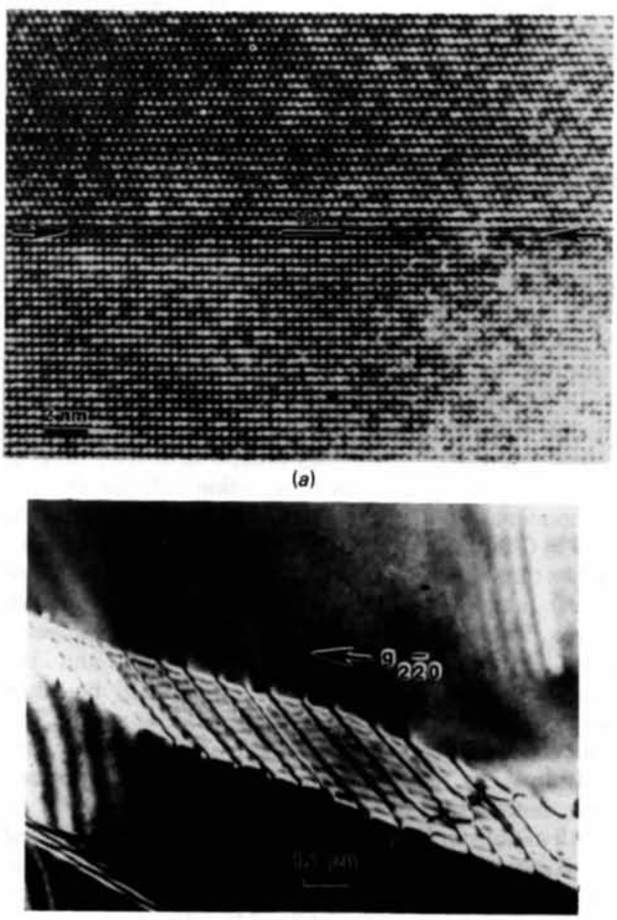

Fig. 14. (*a*) An asymmetric planar interface and (*b*) a small-angle grain boundary, both of which presumably accommodate excessive strain at the twin junctions.

This research is supported by US DOE (grant No. DE-FG02-84ER-45150). The authors would like to thank Professor V. S. Stubican of Pennsylvania State University for kindly donating the specimens used in this study, and the anonymous referee II for useful suggestions.

References

AHTEE, M., GLAZER, A. M. & HEWAT, A. W. (1978). *Acta Cryst.* B**34**, 752–758.

AMELINCKX, S. & VAN LANDUYT, J. (1978). *Diffraction and Imaging Techniques in Materials Science*, edited by S. AMELINCKX, R. GEVERS & J. VAN LANDUYT, pp. 107–152. New York: North-Holland.

BIGGIN, S. & DINGLEY, D. J. (1977). *J. Appl. Cryst.* **10**, 376–385.

BOWMAN, H. L. (1908). *Mineral. Mag.* **15**, 156–176.

BUXTON, D. F., EADES, J. A., STEEDS, J. W. & RACKHAM, G. M. (1976). *Philos. Trans. R. Soc. London Ser.* A, **281**, 171–194.

COUGHANOUR, L. W., ROTH, R. S., MARZULLO, S. & SENNETT, F. E. (1955). *J. Res. Natl Bur. Stand.* **54**, 191–199.

DRAVID, V. P., NOTIS, M. R. & LYMAN, C. E. (1987). *J. Mater. Sci.* **22**, 4546–4549.

ECOB, R. C., SHAW, M. P. PORTER, A. J. & RALPH, B. (1981). *Philos. Mag.* A**44**, 1117–1133.

FOEX, M., TRAVERSE, J. P. & COUTURES, J. (1967). *C. R. Acad. Sci. Sér. C*, **264**, 1837–1840.

GJONNES, J. & MOODIE, A. (1965). *Acta Cryst.* **19**, 65–67.

GLAZER, A. M. (1972). *Acta Cryst.* B**28**, 3384–3392.

GUYMONT, M., GRATIAS, D., PORTIER, R. & FAYARD, M. (1976). *Phys. Status Solidi A*, **38**, 629–636.

International Tables for Crystallography (1983). Vol. A. Dordrecht: D. Reidel. (Present distributor Kluwer Academic Publishers, Dordrecht.)

JONES, P. M., RACKHAM, G. M. & STEEDS, J. W. (1975). *Proc. R. Soc. London Ser. A*, **354**, 197–222.

KAY, H. F. & BAILEY, P. C. (1957). *Acta Cryst.* **10**, 219–226.

KOOPMANS, H. J. A., VAN DE VELDE, G. M. H. & GELLINGS, P. J. (1983). *Acta Cryst.* C**39**, 1323–1325.

MEGAW, H. (1946). *Proc. Phys. Soc. London*, **58**, 133–152.

O'KEEFFE, M. O. & HYDE, B. G. (1977). *Acta Cryst.* B**33**, 3802–3813.

SHELTON, C. G., PORTER, A. J. & RALPH, B. (1983). *Inst. Phys. Conf. Ser.* **68**, 47–49.

STEEDS, J. W. & VINCENT, R. (1983). *J. Appl. Cryst.* **16**, 317–324.

STUBICAN, V. (1986). Abstr., 3rd Int. Conf. Sci. Technol. Zirconia, Tokyo, Japan. In the press.

SUNG, C. M. & WILLIAMS, D. B. (1987). Proc. 45th Annu. Meet. EMSA, edited by G. W. BAILEY, pp. 384–385.

TANAKA, M., SAITO, R. & TSUZUKI, K. (1982). *J. Phys. Soc. Jpn*, **51**, 2635–2640.

VAN TENDELOO, G. & AMELINCKX, S. (1974). *Acta Cryst.* A**30**, 431–440.

VEGAS, A., VALLET-REGI, M., GONZALEZ-CALBET, J. M. & ALARIO-FRANCO, M. A. (1986). *Acta Cryst.* B**42**, 167–172.

WHITE, T. J., SEGALL, R. L., BARRY, J. C. & HUTCHISON, J. L. (1985). *Acta Cryst.* B**41**, 93–98.